

Milliarcsecond Astrometry for the Galilean Moons Using Stellar Occultations

B. E. Morgado, A. R. Gomes-Júnior, F. Braga-Ribas, R. Vieira-Martins, J. Desmars, V. Lainey, E. d'Aversa, D. Dunham, J. Moore, K. Baillié, et al.

▶ **To cite this version:**

B. E. Morgado, A. R. Gomes-Júnior, F. Braga-Ribas, R. Vieira-Martins, J. Desmars, et al.. Milliarcsecond Astrometry for the Galilean Moons Using Stellar Occultations. The Astronomical Journal, 2022, 163, 10.3847/1538-3881/ac6108 . insu-03713323

HAL Id: insu-03713323
https://insu.hal.science/insu-03713323

Submitted on 4 Jul 2022

HAL is a multi-disciplinary open access archive for the deposit and dissemination of scientific research documents, whether they are published or not. The documents may come from teaching and research institutions in France or abroad, or from public or private research centers.

L'archive ouverte pluridisciplinaire **HAL**, est destinée au dépôt et à la diffusion de documents scientifiques de niveau recherche, publiés ou non, émanant des établissements d'enseignement et de recherche français ou étrangers, des laboratoires publics ou privés.



Distributed under a Creative Commons Attribution 4.0 International License

The Astronomical Journal, 163:240 (15pp), 2022 May https://doi.org/10.3847/1538-3881/ac6108
© 2022. The Author(s). Published by the American Astronomical Society.
OPEN ACCESS

Milliarcsecond Astrometry for the Galilean Moons Using Stellar Occultations

B. E. Morgado[1,2,3,6], A. R. Gomes-Júnior[2,4], F. Braga-Ribas[1,2,3,5], R. Vieira-Martins[1,2,6], J. Desmars[7,8], V. Lainey[8], E. D'aversa[9], D. Dunham[10], J. Moore[10], K. Baillié[8], D. Herald[11,12], M. Assafin[2,6], B. Sicardy[3], S. Aoki[13], J. Bardecker[10], J. Barton[10], T. Blank[10], D. Bruns[10], N. Carlson[10], R. W. Carlson[14], K. Cobble[10], J. Dunham[10], D. Eisfeldt[10], M. Emilio[15], C. Jacques[16], T. C. Hinse[17,18], Y. Kim[19,20], M. Malacarne[21], P. D. Maley[10,22], A. Maury[23], E. Meza[24,25], F. Oliva[9], G. S. Orton[14], C. L. Pereira[1,2,5], M. Person[26], C. Plainaki[27], R. Sfair[4,28], G. Sindoni[27], M. Smith[10], E. Sussenbach[29], P. Stuart[10], J. Vrolijk[30], and O. C. Winter[4]

[1] Observatório Nacional/MCTI, R. General José Cristino 77, CEP 20921-400 Rio de Janeiro—RJ, Brazil; morgado.fis@gmail.com
[2] Laboratório Interinstitucional de e-Astronomia—LIneA, Rua Gal. José Cristino 77, Rio de Janeiro, RJ 20921-400, Brazil
[3] LESIA, Observatoire de Paris, Université PSL, CNRS, Sorbonne Université, Université Paris Diderot, Sorbonne Paris Cité, 5 Place Jules Janssen, F-92195 Meudon, France
[4] UNESP—São Paulo State University, Grupo de Dinâmica Orbital e Planetologia, CEP 12516-410, Guaratinguetá, SP, Brazil
[5] Federal University of Technology—Paraná (UTFPR/DAFIS), Rua Sete de Setembro, 3165, CEP 80230-901, Curitiba, PR, Brazil
[6] Universidade Federal do Rio de Janeiro—Observatório do Valongo, Ladeira Pedro Antônio 43, CEP 20.080-090 Rio de Janeiro—RJ, Brazil
[7] Institut Polytechnique des Sciences Avancées IPSA, 63 Boulevard de Brandebourg, F-94200 Ivry-sur-Seine, France
[8] IMCCE, Observatoire de Paris, PSL University, CNRS, Sorbonne Université, Université Lille, 77 Av. Denfert-Rochereau, F-75014 Paris, France
[9] Istituto Nazionale di Astrofisica-Istituto di Astrofisica e Planetologia Spaziali, INAF-IAPS, Rome, Italy
[10] International Occultation Timing Association (IOTA), PO Box 20313, Fountain Hills, AZ 85269, USA
[11] International Occultation Timing Association/European Section, Am Brombeerhag 13, D-30459 Hannover, Germany
[12] Trans-Tasman Occultation Alliance (TTOA), Wellington PO Box 3181, New Zealand
[13] Japan Aerospace Exploration Agency, JAXA, Japan
[14] Jet Propulsion Laboratory, California Institute of Technology, Pasadena, CA, USA
[15] Universidade Estadual de Ponta Grossa (UEPG), Ponta Grossa, Brazil
[16] Observatório SONEAR, Brazil
[17] Institute of Astronomy, Faculty of Physics, Astronomy and Informatics, Nicolaus Copernicus University, Grudziadzka 5, 87-100, Torun, Poland
[18] Chungnam National University, Department of Astronomy and Space Science, 34134, Daejeon, Republic of Korea
[19] Department of Astronomy and Space Science, Chungbuk National University, 28644 Cheongju, Republic of Korea
[20] Chungbuk National University Observatory, Chungbuk National University, 28644 Cheongju, Republic of Korea
[21] Universidade Federal do Espírito Santo, Av. Fernando Ferrari 514, Vitória, ES, 29075-910, Brazil
[22] NASA Johnson Space Center Astronomical Society, Houston, TX, USA
[23] San Pedro de Atacama Celestial Explorations—SPACE, Chile
[24] Comisión Nacional de Investigación y Desarrollo Aeroespacial del Perú - CONIDA, Peru
[25] Observatorio Astronómico de Moquegua—MPC Code W73, Peru
[26] MIT, Cambridge, MA, USA
[27] Agenzia Spaziale Italiana, ASI, Rome, Italy
[28] Institut für Astronomie und Astrophysik, Eberhard Karls Universität Tübingen, Auf der Morgenstelle 10, D-72076 Tübingen, Germany
[29] Pletterijweg Oost, Willemstad, Curaçao, The Netherlands
[30] Space and Nature Aruba Foundation, Aruba, The Netherlands
Received 2022 January 19; revised 2022 March 8; accepted 2022 March 14; published 2022 April 28

Abstract

A stellar occultation occurs when a Solar System object passes in front of a star for an observer. This technique allows the sizes and shapes of the occulting body to be determined with kilometer precision. In addition, this technique constrains the occulting body's positions, albedos, densities, and so on. In the context of the Galilean moons, these events can provide their best ground-based astrometry, with uncertainties in the order of 1 mas (~3 km at Jupiter's distance during opposition). We organized campaigns and successfully observed a stellar occultation by Io (JI) in 2021, one by Ganymede (JIII) in 2020, and one by Europa (JII) in 2019, with stations in North and South America. We also re-analyzed two previously published events: one by Europa in 2016 and another by Ganymede in 2017. We then fit the known 3D shape of the occulting satellite and determine its center of figure. This resulted in astrometric positions with uncertainties in the milliarcsecond level. The positions obtained from these stellar occultations can be used together with dynamical models to ensure highly accurate orbits of the Galilean moons. These orbits can help when planning future space probes aiming at the Jovian system, such as JUICE by ESA and Europa Clipper by NASA. They also allow more efficient planning of flyby maneuvers.

Unified Astronomy Thesaurus concepts: Occultation (1148); Galilean satellites (627); Astrometry (80)

1. Introduction

The progress in the astrometry and modeling of the orbits of planetary satellites in the last decade has enabled the accurate estimation of tidal effects in natural satellites and their primaries (Lainey et al. 2009, 2012, 2017). However, these studies need accurate observations that are spread over a significant period of time to provide essential constraints on short and long-term dynamics, up to formation processes (Charnoz et al. 2011; Crida & Charnoz 2012).

Accurate orbits also help in the preparation of space missions targeting these systems (Dirkx et al. 2016, 2017). ESA's JUICE

Original content from this work may be used under the terms of the Creative Commons Attribution 4.0 licence. Any further distribution of this work must maintain attribution to the author(s) and the title of the work, journal citation and DOI.

Table 1
Occulted Star's Parameters for Each Observed Event as Obtained from Gaia EDR3

Ev.	Date and time UTC yyyy-mm-dd hh:mm:ss	Gaia EDR3 source identifier	R.A.[a] hh mm ss.sss (mas)	Decl.[a] dd mm ss.sss (mas)	G mag
a	2021-04-02 10:24:00	6841731655255386240	$21^h43^m04\overset{s}{.}38938$ (0.24)	$-14°23'58\overset{''}{.}5337$ (0.16)	5.82
b	2020-12-21 00:49:00	6866303987792105856	$20^h09^m33\overset{s}{.}49678$ (0.12)	$-20°35'38\overset{''}{.}7273$ (0.08)	7.38
c	2019-06-04 02:26:00	4114900624661072256	$17^h16^m59\overset{s}{.}88385$ (0.08)	$-22°28'06\overset{''}{.}8486$ (0.04)	9.14
d	2017-03-31 06:44:00	3629528535155010432	$13^h12^m15\overset{s}{.}54298$ (0.03)	$-05°56'48\overset{''}{.}7523$ (0.02)	9.51
e	2016-04-13 11:57:00	3866368596817620352	$11^h03^m41\overset{s}{.}27681$ (0.02)	$+07°34'54\overset{''}{.}6795$ (0.02)	6.99

Note.
[a] The star's coordinates (R.A. and decl.) and their uncertainties were propagated to the occultation epoch with the formalism proposed by Butkevich & Lindegren (2014) using the parameters (i.e., proper motion, parallax, radial velocity, etc) from Gaia EDR3 (Gaia Collaboration et al. 2021), corrected as suggested by Cantat-Gaudin & Brandt (2021).

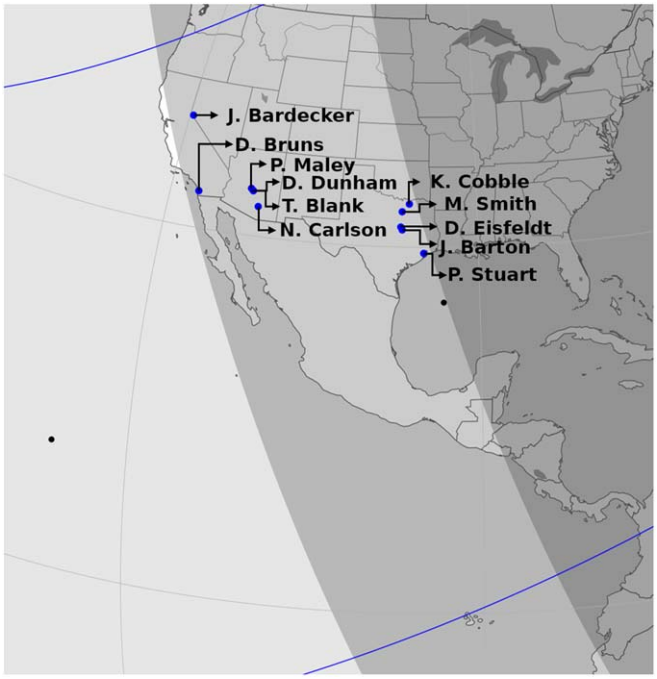


Figure 1. Map of the stellar occultation by Ganymede in 2020 December 21 as observed in the United States of America. The blue dots represent the observational stations that participated in this campaign, each station indicated by its lead observer's name. The blue lines represent the shadow limits, and the black dots are the center of the shadow, separated by one minute. The shades of gray represent the night (dark gray), twilight, and day (light gray) part of the globe.

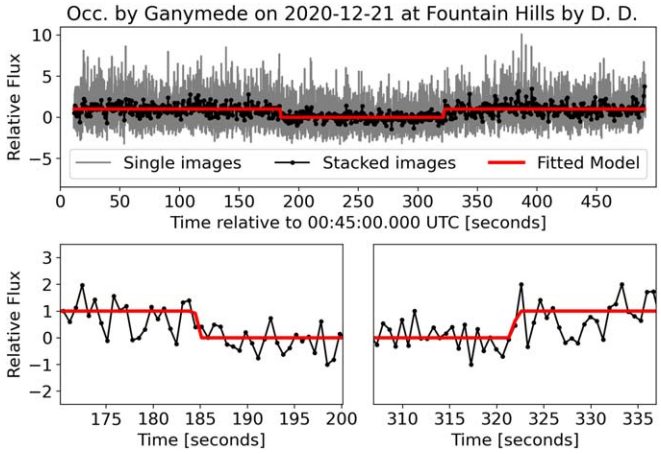


Figure 2. Normalized light curve obtained by D. Dunham of the occultation by Ganymede on 2020 December 21. The gray line shows the photometry of the single images, while the black dots represent the photometry after the stacking of 20 images. The red line represents the fitted model. The bottom panels contain a zoom-in on 30 s centered on the immersion and emersion times. We highlight the need for the stacking procedure to detect the occultation in this data set. All of the light curves used in this work can be found in Appendix B.

and NASA's Europa Clipper missions are scheduled to be launched this decade (the 2020s) for the Jovian system. Therefore, accurate ground-based astrometry of natural satellites is important for these missions.

In the CCD era, straightforward classical astrometry cannot be used for all of the natural satellites. The case of Galilean moons is a critical example because Jupiter's brightness in the Field of View (FoV) would quickly saturate the CCD, thus providing positions with uncertainties that range between 100 and 150 milliarcseconds (mas; Kiseleva et al. 2008). This scenario motivates the search for alternative methods for the astrometry of these satellites, such as the mutual phenomena events (Aksnes & Franklin 1976; Aksnes et al. 1984; Emelyanov 2009; Arlot et al. 2014; Saquet et al. 2018; Morgado et al. 2019c, and references therein), mutual approximations (Morgado et al. 2016, 2019a), radar astrometry (Brozović et al. 2020), and stellar occultations (Morgado et al. 2019b), among others.

A stellar occultation occurs when a Solar System object passes in front of a star for an observer. This technique allows the sizes and shapes to be determined with kilometer precision. In addition, it can obtain the object's position, albedo, density, and so on (Sicardy et al. 2011; Gomes-Júnior et al. 2022, and references therein). It is essential to have good ephemerides of the occulting objects and a good knowledge of the occulted star's position to predict stellar occultations accurately. Thanks to the Gaia Mission (Gaia Collaboration et al. 2016a) and its catalogs—Gaia DR1, DR2, and EDR3 (Gaia Collaboration et al. 2016b, 2018, 2021)—the positions of the stars are known at mas level.

Stellar occultations of the Galilean moons can provide shapes and sizes with uncertainties that are comparable with those of space probe images but are not affected by albedo variations on the satellite's surface, which is highly influenced by the solar phase angle. From an astrometric point of view, these events can provide the best ground-based astrometry of these moons, with uncertainties in the order of 1 mas (~3 km at Jupiter distance at opposition). This accuracy is usually one order of magnitude better than other methods (Morgado et al. 2019b).

Historically, stellar occultations by Galilean satellites have been recorded since 1971 using photoelectric photometers (Hubbard & van Flandern 1972; Carlson et al. 1973). Nonetheless, few events

Table 2
Fitted Times Obtained for Each Light Curve with a Positive Detection

#	Station	Immersion Time UTC	Emersion Time UTC	Chord Length (s)	χ^2_{pdf}
	(a) 2021-04-02—Stellar occultation by (501) Io				
1	Savaneta, Aruba—J. Vrolijk	10:19:54.843 (0.420)	10:20:45.762 (1.278)	50.919 (1.698)	0.804
2	Jan Thiel, Curaçao—E. Sussenbach	10:19:50.975 (0.036)	10:20:56.142 (0.036)	65.167 (0.072)	0.755
	(b) 2020-12-21—Stellar occultation by (503) Ganymede				
1	Gardnerville, USA—J. Bardecker	00:48:04.694 (0.480)	00:49:42.632 (0.590)	103.051 (1.212)	0.973
2	San Diego, USA—D. Bruns	00:47:58.782 (0.888)	00:50:08.367 (1.273)	129.585 (2.161)	0.877
3	Carefree, USA—P. Maley	00:48:04.738 (0.663)	00:50:20.773 (0.304)	136.035 (0.967)	0.864
4	Fountain Hills, USA—D. Dunham	00:48:04.736 (0.687)	00:50:21.845 (0.500)	137.109 (1.188)	0.820
5	Fountain Hills, USA—T. Blank	00:48:06.403 (0.751)	00:50:22.689 (0.513)	136.286 (1.264)	1.109
6	Tucson, USA—N. Carlson	[a]	00:50:28.670 (2.654)	>117.670[b]	0.980
7	Princeton, USA—K. Cobble	00:48:17.567 (0.778)	00:50:52.657 (0.242)	155.090 (1.020)	0.907
8	Colleyville, USA—M. Smith	00:48:16.411 (0.774)	00:50:49.259 (2.548)	155.257 (1.246)	0.916
9	Waco, USA—D. Eisfeldt	00:48:17.664 (1.193)	00:50:54.283 (1.532)	152.515 (0.699)	1.071
10	Lorena, USA—J. Barton	00:48:18.202 (0.131)	00:50:54.556 (0.293)	156.354 (0.424)	0.922
11	Clear Lake Shores, USA—P. Stuart	00:48:20.539 (0.468)	00:50:59.476 (0.560)	158.938 (1.028)	0.866
	(c) 2019-06-04—Stellar occultation by (502) Europa				
1	CP Cambrune, Peru—E. Meza	02:28:05.033 (0.044)	02:29:14.311 (0.040)	069.278 (0.084)	0.891
	(d) 2017-03-31—Stellar occultation by (502) Europa				
1	OPD—Brazópolis, Brazil—M. Assafin	06:38:28.550 (0.750)	06:41:06.150 (0.240)	157.600 (0.990)	[c]
2	Foz do Iguaçu, Brazil—D. I. Machado	06:39:26.070 (0.770)	06:41:21.590 (1.070)	115.520 (1.840)	[c]
3	San Pedro de Atacama, Chile—A. Maury	06:40:38.190 (1.200)	06:42:22.850 (0.340)	104.660 (1.540)	[c]
	(e) 2016-04-13—Stellar occultation by (503) Ganymede				
1	IRTF—Maunakea, Hawaii—E. D'Aversa	11:51:33.722 (1.218)	11:56:20.938 (1.239)	287.216 (2.457)	0.965
2	SOAO—Sobaeksan, South Korea—T. C. Hinse	11:58:02.028 (2.222)	12:01:51.064 (2.218)	229.039 (4.440)	0.579

Notes.
[a] Due to observational issues, the recording started after the immersion time.
[b] The minimum chord length was calculated based on the start of acquisition (00:48:31.334 UTC).
[c] Values from Morgado et al. (2019b).

have since been observed and they were organized in the Small Bodies Occultations Database[31] using the reduction process described in Herald et al. (2020). These events are rare because only stars with magnitude V brighter than 11.5 will provide a magnitude drop higher than 0.5%.

Between 2019 and 2021, Jupiter was crossing a very dense star region, with the Galactic center as its background (Gomes-Júnior et al. 2016). The probability of a Jovian Moon to occult a bright star increased dramatically during this epoch, which allowed the organization of observational campaigns to observe such events. This passage will occur again only in 2030.

Here, we will detail the analysis of three stellar occultations by Galilean moons. These events were: (i) the double chord stellar occultation by Io (JI) on 2021 April 2; (ii) the multi-chord event by Ganymede (JIII) on 2020 December 21; and (iii) the single-chord event by Europa (JII) on 2019 April 6. The first was favorable to Central and South America with positive detections on Aruba and Curacao. The second was favorable to the USA during the twilight. The third was observable from South America, with a positive detection on Peru.

We will also re-analyze two previously published stellar occultations by Galilean moons to provide new astrometry in the Gaia EDR3 reference frame. They were the stellar occultation by Europa on 2017 March 31 published by Morgado et al. (2019b) and the occultation by Ganymede on 2016 April 13 that was previously analyzed by D'Aversa et al. (2017). This project aims to obtain the astrometric position of the occulting Galilean Moon at the occultation instant for all of the listed events.

This paper is organized as follows. In Section 2, we described the analysis process, the pipeline, and the software used. Section 3 contains the observational details and our results. We give our final remarks in Section 4.

Table 3
Sub-observer Coordinates for the Occulting Satellite on the Event Instant

Ev.	Sat.[a]	Date and time UTC yyyy-mm-dd hh:mm:ss	ϕ deg.	λ deg.
a	501	2021-04-02 10:24:00	196.625	+0.123
b	503	2020-12-21 00:49:00	130.072	−1.014
c	502	2019-06-04 02:26:00	144.983	−3.057
d	502	2017-03-31 06:44:00	270.041	−3.359
e	503	2016-04-13 11:57:00	135.783	−1.574

Note: For (501) Io, we used the complex 3D shape as published by White et al. (2014). For (502) Europa, we used the triaxial shape with axis $a > b > c$ equals to 1562.6, 1560.3 and 1559.5 km as published by Nimmo et al. (2007). For (503) Ganymede, we used the triaxial ellipsoid with axis 2634.6, 2633.0 and 2631.4 km published by Zubarev et al. (2015).
[a] 501 stands for Io, 502 for Europa and 503 for Ganymede.

[31] https://sbn.psi.edu/pds/resource/occ.html

2. Data Analysis

We used the stacking consecutive images technique and classical photometric pipelines to extract the occultation light curves, as detailed in Section 2.1. Abrupt opaque edge models, including the effects of diffraction, finite bandwidth, exposure time, and stellar diameter, were fitted to the star's disappearance and reappearance behind the satellite at the various stations defined by the occultation chords (Section 2.2). As described in Section 2.3, we then used the known 3D shape of the object to find its limb and then fitted this limb to the occultation chords. From this fit, we obtained the center of the figure and determined the astrometry of the occulting satellite.

2.1. Analysis of Images and Aperture Photometry

The images obtained in the observational campaigns were saved in different formats. The first step was to convert them to `.fits` files. From `.avi` to `.fits`, we used a proprietary PYTHON software that is based on `astropy v4.0.1` (Astropy Collaboration et al. 2013). When calibration images (bias, dark and flat-field) were available, we used them to correct the original images using standard procedures of the Image Reduction and Analysis Facility (`IRAF;` Tody 1986).

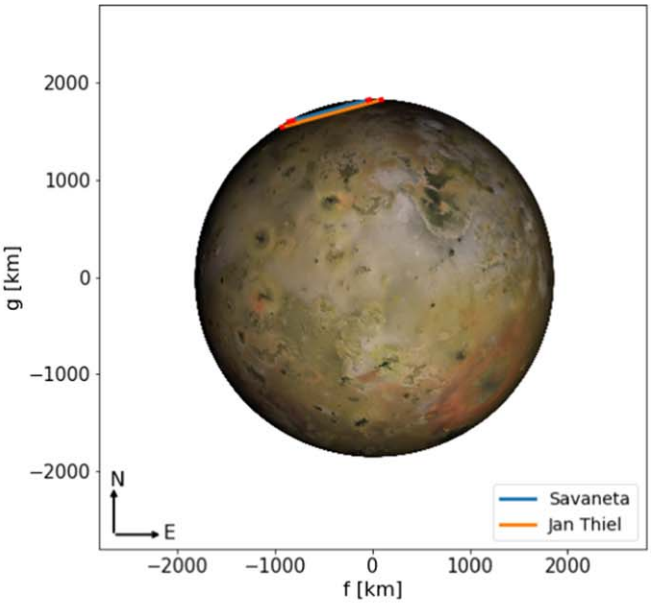
When observing the Galilean satellites, one should take particular care not to saturate the CCD image, which will quickly happen due to Jupiter's brightness. Meanwhile, stellar occultations by bright objects, such as the Galilean moons (visual magnitude about 5.5), will usually have small magnitude drops (mag. ∼11 star will have magnitude drop about 1.0%). Consequently, saturation would usually happen before an adequate Signal to Noise ratio (S/N) to show the magnitude drop can be achieved. Whenever the magnitude drop was too small to be measured in the single images, we used the stacking consecutive images technique to increase the images' S/N at the cost of the time resolution.

Before stacking the images, we measured the target centroid (x, y) in the images with a 2D circular symmetric Gaussian fit over pixels within one full-width at half-maximum (FWHM ∝seeing) from the center using the Platform for Reduction of Astronomical Images Automatically (`PRAIA,` Assafin et al. 2011). The alignment consists of vertical and horizontal shifts for each image $(\Delta x, \Delta y)$ relative to a chosen reference image; in our case, the first images of each data set. After the alignment between the images, the stack was done with proprietary software in PYTHON (Morgado et al. 2019b, Appendix A). We manually chose the number of stacked images to get the best compromise between S/N and time resolution.

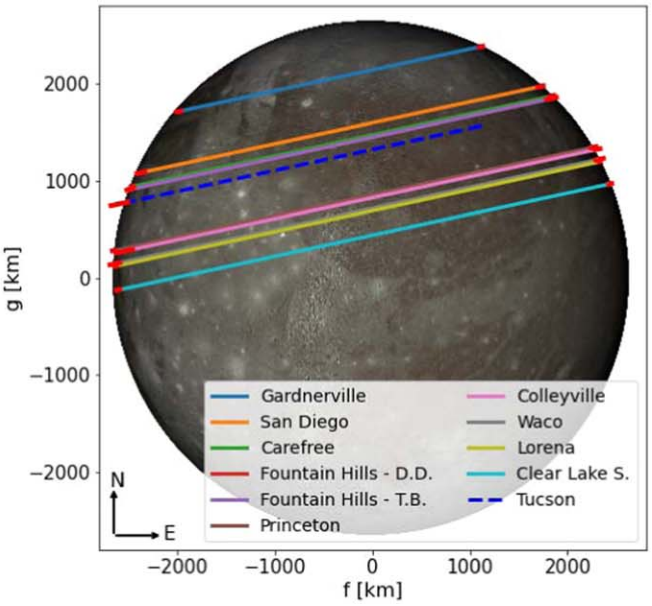
The next step was aperture photometry of the target and calibration objects. We used the PRAIA package for this step. Note that during the occultation, the star and the satellite are blended in the same aperture. This combined flux was normalized to unity outside the occultation, using a polynomial fit before and after the event. Finally, nearby satellites were used as photometric calibrators to correct for low-frequency sky transparency fluctuations.

2.2. Times and Projection in the Sky Plane

With the normalized light curves, we obtained the immersion (disappearance) and emersion (reappearance) times using the Stellar Occultation Reduction and Analysis (`SORA,` Gomes-Júnior et al. 2022) package. The fitted occultation model



(a) Occultation by 501 on 02/04/2021

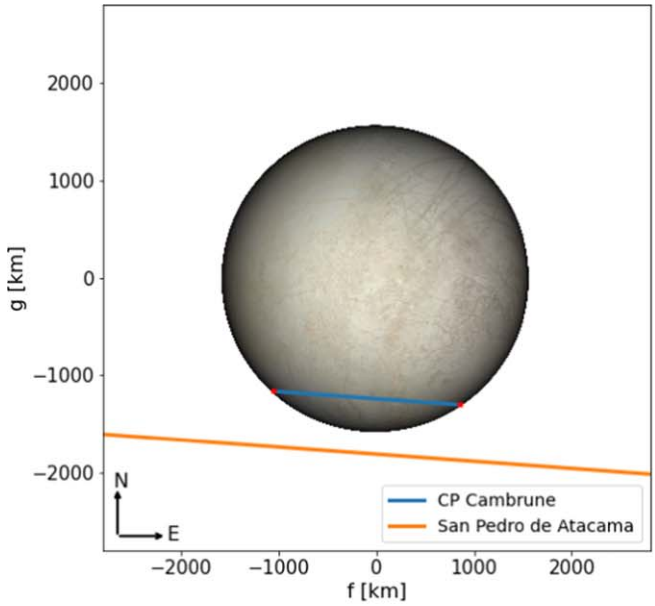


(b) Occultation by 503 on 21/12/2020

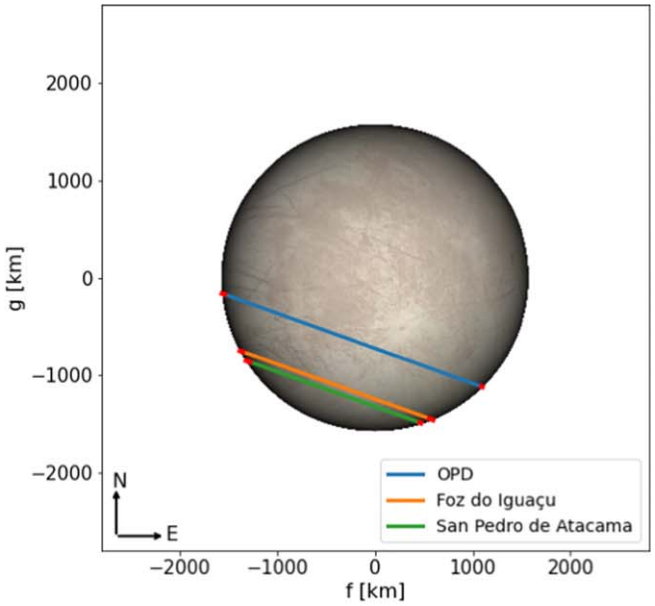
Figure 3. We fitted the limb of the Galilean satellites to the stellar occultation chords. In panel (a), we show the stellar occultation by Io on 2021 April 2 observed from South America. In panel (b), we show the stellar occultation by Ganymede on 2020 December 21 observed from North America. The red segment in the extremities stands for the 1σ error bar in each disappearance and reappearance time. We note that some redundant chords may be visually indistinguishable.

considers a sharp-edge occultation model convolved with Fresnel diffraction, stellar diameter (projected at the body distance), CCD bandwidth, and finite integration time.

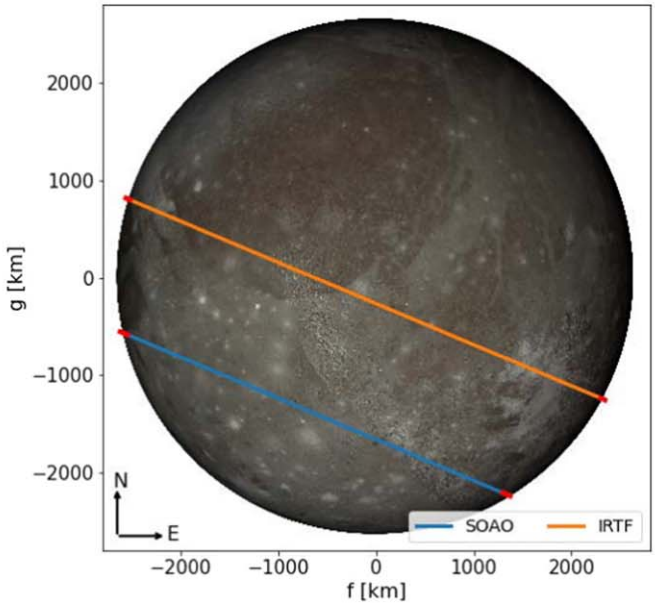
Using the Jovian ephemeris (here, the `jup365` and `de440`), the Gaia EDR3 star positions propagated to the event epoch, and the observer's position on Earth (latitude, longitude, and height), each disappearance or reappearance time is associated with a stellar position relative to the occulting satellite in the sky plane (f, g). We expressed this position in kilometers, f



(e) Occultation by 502 on 04/06/2019



(f) Occultation by 502 on 31/03/2017



(g) Occultation by 503 on 2016-04-13

Figure 4. Same as Figure 3 for events: (c) by Europa on 2019 June 4 observed from South America; (d) by Europa on 2017 March 31 observed from South America and previously published by Morgado et al. (2019b); (e) by Ganymede on 2016 April 13 observed from North America and previously published by D'Aversa et al. (2017).

(resp. g) being counted positively toward the local east (resp. north) celestial direction. The pair of positions from the same site describes a chord.

2.3. Limb Fit and Astrometric Result

Each chord extremity is a point at which we can fit the limb of the figure. Here, we considered the satellite's 3D size and shape to be known, as observed by many space missions. For instance, the (501) Io complex 3D shape was published by White et al. (2014). Meanwhile, the (502) Europa global shape was studied and published by Nimmo et al. (2007) and (503) Ganymede was studied by Zubarev et al. (2015).

Using the rotational elements of the Galilean satellites (i.e., pole coordinates, direction of the prime meridian, and its time variation) as provided by Archinal et al. (2018), we calculated their space orientation as seen from Earth at the occultation epoch. In other words, we determined the geocentric sub-observer latitude (ϕ) and longitude (λ) at the occultation instant.

After orienting the 3D shape in the sky plane, we obtain its limb and use it to fit the center of the figure, considering the observed chords. This fit was done using a Monte Carlo approach with uniform distributions of initial guesses to test a vast number of simulated central positions ($\sim$1.000.000), for

Table 4
Astrometric Positions for Each Event

Event	Satellite[a]	Date and Time UTC yyyy-mm-dd hh:mm:ss	R.A.[b] hh mm ss.sss (mas)	Decl.[b] dd mm ss.sss (mas)
a	501	2021-04-02 10:24:00.000	$21^h43^m04\overset{s}{.}37583$ (1.1)	$-14°23'58\overset{''}{.}1536$ (0.7)
b	503	2020-12-21 00:49:00.000	$20^h09^m33\overset{s}{.}56022$ (0.9)	$-20°35'38\overset{''}{.}0137$ (1.7)
c	502	2019-06-04 02:26:00.000	$17^h16^m59\overset{s}{.}89400$ (1.1)	$-22°28'06\overset{''}{.}5375$ (1.1)
d	502	2017-03-31 06:44:00.000	$13^h12^m15\overset{s}{.}54781$ (1.9)	$-05°56'48\overset{''}{.}6987$ (1.6)
e	503	2016-04-13 11:57:00.000	$11^h03^m41\overset{s}{.}32089$ (4.1)	$+07°34'55\overset{''}{.}6614$ (4.7)

Notes.
[a] 501 stands for Io, 502 for Europa and 503 for Ganymede.
[b] These positions assume the EDR3 star positions given in Table 1.

Table 5
Offsets in Mas Between the Obtained Positions for Each Event and Different Ephemerides

Event	Uncertainties (mas)		$O-C_1$ (mas)		$O-C_2$ (mas)		$O-C_3$ (mas)		$O-C_4$ (mas)	
	ΔRA	ΔDec	ΔRA	ΔDec	ΔRA	ΔDec	ΔRA	ΔDec	ΔRA	ΔDec
a	1.1	0.7	+05.5	−02.9	−01.3	−01.5	+06.7	−05.1	−00.1	−03.7
b	0.9	1.7	−04.2	−00.1	−03.4	−01.6	−03.2	−02.4	−02.4	−04.0
c	1.1	1.1	−04.1	−03.1	−08.0	−16.8	−03.9	−05.8	−07.8	−19.5
d	1.9	1.6	−00.2	−00.3	−06.3	−10.6	+00.5	+00.3	−05.7	−10.0
e	4.1	4.7	−02.3	+07.5	−02.2	+09.5	−01.1	+09.4	−01.0	+11.4

Note. C_1 is using ephemeris `de440` and `jup365`; C_2 is `de440` and `NOE-5-2021`; C_3 is ephemeris `INPOP19` and `jup365`; C_4 is `INPOP19` and `NOE-5-2021`.

which we compute chi-squared statistics using Equation (1).

$$\chi^2 = \sum_{i=1}^{N} \frac{(r_i - r'_i)^2}{\sigma_{ri}^2} \quad (1)$$

were σ_{ri} stands for the radial component of the uncertainty in each chord extremity. With this approach, we determine the fitted value as the one that minimizes the χ^2, and we determine the marginal 1σ error bar considering the region where $\chi^2 < \chi^2_{\min} + 1$, as discussed in Press et al. (1992).

The center positions (f_c, g_c) can be converted to an astrometric offset between the occulting object's center of figure and the star's position ($\Delta\alpha \cos\delta$, $\Delta\delta$). The Gaia EDR3 catalogs provide the star's positions at sub-mas level precision (Gaia Collaboration et al. 2021). This allows us to calculate astrometric positions of the occulting object with high accuracy. We highlight that the orientation of the coordinate axes is the same as the ICRS, and we set the origin in the geocenter. The uncertainties of the positioning stem from the uncertainties of the fitted center (σf_c, σg_c) and the uncertainties in the star's position propagated to the occultation epoch. Note that the resulting uncertainties are usually at mas level, corresponding to a few kilometers at Jupiter's distance, where 1 mas correspond to ∼3 km at opposition.

The reduction pipeline does not consider any correction for relativistic deflection by the Sun or other major bodies on the relative position between the occulting satellite and the occulted star.

3. Observational Campaigns and Results

The passage of Jupiter on crowded stellar fields created some opportunities to observe stellar occultations of bright stars by the Galilean moons. Between 2019 and 2021, we organized six observational campaigns, three of which resulted in data sets with at least one positive detection. Some of these campaigns involved stars with magnitudes fainter than mag 10, and even the stacking consecutive images technique does not allow us to retrieve any positive detection.

The observational campaigns were organized in collaboration with citizen astronomers spread throughout South and North America, including communities such as the International Occultation Timing Association (IOTA/USA[32]). We organize the prediction details of the successful campaigns in Table 1. This table shows the occultation date and time; the occulted star's Gaia EDR3 source identifier; and its R.A., decl., and G magnitude. The star's positions were propagated to the occultation epoch using the rigorous stellar motion described by Butkevich & Lindegren (2014). We also corrected from systematic error in the star's proper motion of Gaia EDR3, as suggested by Cantat-Gaudin & Brandt (2021). We highlight that there are no Gaia flags about duplicity or strange astrometrical behavior for the stars listed here.

Details about the observational stations that participated in each campaign can be found in Appendix A. As an example, Figure 1 shows the map of the occultation by Ganymede on 2020 December 21. The blue lines represent the size limit of Ganymede. The black dots represent the body's center for a given time, each separated by one minute. The blue dots are the eleven stations that observed this event, here represented by the name of the leading observer. In this map, the shades of gray represent the night, twilight, and day part of the globe.

As mentioned in Section 2.1 all of the images in the data sets were analyzed using our pipeline, resulting in light curves such as the one shown in Figure 2. In gray, we see the light flux of every single image, in black the light curve of the stack of 20

[32] https://occultations.org/

consecutive images, and in red the fitted occultation model. Each light curve was analyzed, and the immersion and emersion times were determined as mentioned in Section 2.2. Table 2 contains the obtained UTC times (immersion and emersion), their uncertainties in seconds, and the minimum chi-squared per degree of freedom (χ^2_{pdf}) obtained for each observational station. All of the obtained light curves can be found in Appendix B.

The spectroscopy obtained at the NASA Infrared Telescope Facility (IRTF) using the SpeX[33] (Rayner et al. 2003) instrument at Maunakea needed some additional analysis. This data set consisted of several spectra, each ranging between 0.9 and 2.5 microns, and obtained with a temporal resolution of about 2.8 s. Because it does not have any additional object in the FoV, it was impossible to calibrate the target's flux for sky fluctuations. We were able to overcome this issue by integrating the fluxes within bands Y (between 960—1080 microns), J (1113—1327 microns), H (1476—1784 microns), and K (1995—2385 microns) and then obtaining the color light curves considering the flux ratios within bands. This methodology allows the occultation instants to be determined, even though the sky transparency was not ideal. This was possible because the sky transparency is attenuated because it affects the analyzed bands similarly, and the colors of the target star (mag H − mag J = −0.37) differ from Ganymede's (mag H − mag J = +0.10). Appendix C contains the detailed analysis of the IRTF observations.

The 3D shape was then projected to the occultation instant, using the methodology presented in Section 2.3. The sub-observer latitude (ϕ) and longitude (λ) for each occultation can be found in Table 3.

The chords for each occultation are then combined, and we fit the limb of the figure as explained in Section 2.3. Figures 3 and 4 contain the chords and the fitted 3D limb, where each panel stands for an occultation. The obtained astrometric positions are organized in Table 4.

Our results consist of geocentric astrometric positions with uncertainties in the mas level. Table 5 contains the differences between the observed positions and different geocentric ephemeris.

The 3D models that we have used here for Europa and Ganymede are based on triaxial ellipsoids representing the global shapes of these satellites, meaning that topographic features were not taken into consideration. Nonetheless, based on space-mission data, the expected topographic features of these satellites ranges below 1 km for Europa and 2 km for Ganymede (Thomas et al. 1997; Nimmo et al. 2007; Zubarev et al. 2015). Furthermore, these values are smaller than the uncertainties obtained in the chord's extremities.

All of the observations for the campaigns between 2019 and 2021 went through our entire reduction pipeline. Meanwhile, the re-analysis of the occultation observed in 2017 March 31 and published by Morgado et al. (2019b) started with the times that were already published, so no photometry and time determination was done in the context of this project. For the occultation observed in 2016 April 13, the photometric analysis was done previously by D'Aversa et al. (2017), the light curves were then included in our pipeline, and the disappearance and reappearance times were determined.

[33] http://irtfweb.ifa.hawaii.edu/~spex/

4. Final Remarks

Between 2019 and 2021, we organized and observed stellar occultation campaigns by Galilean moons. Citizen astronomers did many of the observations reported here with small aperture telescopes. These campaigns aimed to obtain positions with uncertainties in the mas level.

Stacking consecutive images techniques were used to improve the S/N ratio, thus emphasizing the low magnitude drop of the occultation. The known 3D shape and size of the Galilean satellites were used here. They were oriented using the sub-observer angles and the formalism presented by Archinal et al. (2018).

From the six organized campaigns, three had at least one positive detection. We also revisited two other stellar occultations that were previously published by Morgado et al. (2019b) and D'Aversa et al. (2017), now using the Gaia EDR3 stellar catalog. This project resulted in five positions with a typical uncertainty below 2 mas (∼6 km at Jupiter distance). These precise positions also allow us to identify significant offsets in the ephemerides.

The obtained positions reported here can be used to reconsider the accuracy of the ephemerides (for both Jupiter and its moons) that are currently used to prepare JUICE and Europa Clipper space missions. Moreover, it has been demonstrated that both missions will face an almost ill-posed problem during radio-science data inversion because of their lack of Io's flybys (Dirkx et al. 2017). The present paper demonstrates the huge potential of stellar occultations observed from the ground to mitigate this issue. Another key aspect of stellar occultations is to provide information on the center of figure of the moons, while radio-science data are sensitive to their center of mass. This shift is unknown for most Solar system objects but could be quantified by merging radio-science and stellar occultation data. Moreover, this should motivate observers worldwide to invest time and energy in observing these occultations by the Galilean satellites. Last, but not least, the current data can evidently be used to improve the current estimations of tidal dissipation within Jupiter and Io (Lainey et al. 2009).

This work was carried out within the "Lucky Star" umbrella that agglomerates the efforts of the Paris, Granada, and Rio teams, which is funded by the European Research Council under the European Community's H2020 (ERC grant Agreement No. 669416). This research made use of SORA, a python package for stellar occultations reduction and analysis, developed with the support of ERC Lucky Star and LIneA/Brazil, within the collaboration of Rio-Paris-Granada teams. This work has made use of data from the European Space Agency (ESA) mission Gaia (https://www.cosmos.esa.int/gaia), processed by the Gaia Data Processing and Analysis Consortium (DPAC, https://www.cosmos.esa.int/web/gaia/dpac/consortium). Part of this research is supported by INCT do e-Universo, Brazil (CNPQ grants 465376/2014-2). This work was supported by CNES, focused on Juice. Based in part on observations made at the Laboratório Nacional de Astrofísica (LNA), Itajubá-MG, Brazil. The following authors acknowledge the respective (i) CNPq grants: B.E.M 150612/2020-6; F.B.-R. 314772/2020-0; R.V.-M. 304544/2017-5, 401903/2016-8; M.A. 427700/2018-3, 310683/2017-3, 473002/2013-2; R.S. and O.C.W. 305210/2018-1. (ii) CAPES/Cofecub grant: B.E.M.

394/2016-05. (ii) FAPERJ grants: M.A. E-26/111.488/2013. (iii) FAPESP grants: A.R.G.Jr. 2018/11239-8; R.S. and O.C.W. 2016/24561-0. The Italian coauthors thank ASI and INAF for the financial support through the "Accordo ASI-INAF n. 2018-25-HH.0". The Infrared Telescope Facility is operated by the University of Hawaii under contract NNH14CK55B with the National Aeronautics and Space Administration. We express special thanks to Bobby Bus as support astronomer for IRTF observations. The Sobaeksan Observatory facility SOAO is managed by the Korean Astronomy and Space Science Institute (KASI). A portion of this research was carried out at the Jet Propulsion Laboratory, California Institute of Technology, under a contract with the National Aeronautics and Space Administration (80NM0018D0004). T.C.H. and Y.K. would like to thank the staff at the SOAO observatory for fruitful discussions on astronomical data presented in this paper. R.S. acknowledges support by the DFG German Research Foundation project 446102036. R.S. and O.C.W. thanks the Brazilian Federal Agency for Support and Evaluation of Graduate Education (CAPES), in the scope of the Program CAPES-PrInt, process number 88887.310463/2018-00, International Cooperation Project number 3266. This research received financial support from the National Research Foundation (NRF; No. 2019R1I1A1A01059609). This study was financed in part by the Coordenação de Aperfeiçoamento de Pessoal de Nível Superior—Brasil (CAPES) - Finance Code 001.

Appendix A
Observational Circumstance

Table 6 summarizes the observational circumstances of each station for the four stellar occultations that are presented here (i.e., name of station, coordinates, observers, telescope aperture, detector, band, exposure and cycle times, and the light-curve root mean square (rms) noise). The status of each observation is mentioned (positive or negative detection). Overcast weather and instrumental issues are also indicated. The information relative to the occultation by Europa in 2017, March 31st, was not added to this table because it can be found in Morgado et al. (2019b).

Table 6
Observational Stations, Technical Details, and Circumstance for the Stellar Occultations on this Project

Status Station Country	Longitude Latitude Altitude	Observers	Telescope Aperture CCD Timing	Single Cycle Time (s) Stacked Cycle Time (s)	Light Curve rms
(a) 2021-04-02—Stellar occultation by (501) Io					
Positive Savaneta Aruba	69° 57′ 04.0″ W 12° 27′ 10.8″ N 17 m	J. Vrolijk	20.3 cm ZWO ASI224MC NTP	0.026 …	0.504
Positive Jan Thiel Curaçao	68° 52′ 23.0″ W 12° 05′ 37.0″ N 18 m	E. Sussenbach	27.9 cm ZWO ASI462MC NTP	0.095 …	0.086
Weather overcast CP Cambrune Peru	70° 40′ 42.5″ W 16° 49′ 41.3″ S 3305 m	E. Meza	100.0 cm ZWO ASI178MM GPS	… …	…
Daylight Curitiba Brazil	49° 20′ 23.7″ W 25° 26′ 10.4″ S 935 m	F. Braga-Ribas	20.3 cm QHY174-GPS GPS	… …	…
(b) 2020-12-21—Stellar occultation by (503) Ganymede					
Positive Gardnerville USA	119° 40′ 20.3″ W 38° 53′ 23.5″ N 1524 m	J. Bardecker	30.5 cm Watec 910HX IOTA-VTI	0.033 0.667	0.905
Positive San Diego USA	117° 09′ 37.0″ W 32° 56′ 16.7″ N 81 m	D. Bruns	27.9 cm ZWO ASI1600MM SNTP	0.100 1.000	0.680
Positive Carefree USA	111° 57′ 08.0″ W 33° 48′ 42.9″ N 654 m	P. Maley	20.0 cm Night Eagle Astro IOTA-VTI	0.033 0.667	0.874
Positive Fountain Hills USA	111° 43′ 39.0″ W 33° 37′ 28.3″ N 520 m	D. Dunham J. Dunham	12.7 cm Night Eagle Astro IOTA-VTI	0.033 0.667	0.727
Positive Fountain Hills USA	111° 43′35.3″ W 33° 37′ 21.2″ N 515 m	T. Blank	35.6 cm Watec 910HX IOTA-VTI	0.033 0.667	0.931
Positive Tucson USA	111° 01′ 48.5″ W 32° 25′ 00.0″ N 825 m	N. Carlson	23.5 cm Night Eagle Astro Visual	0.040 0.800	1.126
Positive Princeton USA	96° 29′ 19.6″ W 33° 29′ 30.7″ N 175 m	K. Cobble	12.7 cm QHY 174 GPS GPS	0.034 0.669	0.628
Positive Colleyville USA	97° 08′ 20.8″ W 32° 52′ 50.2″ N 160 m	M. Smith	12.7 cm Watec 902H IOTA-VTI	0.033 0.667	0.857
Positive Waco USA	97° 14′ 59.8″ W 31° 37′ 44.6″ N 161 m	D. Eisfeldt	20.3 cm Night Eagle Astro IOTA-VTI	0.033 0.667	0.893
Positive Lorena USA	97° 05′ 04.6″ W 31° 24′ 47.9″ N 134 m	J. Barton	31.7 cm Watec 902H IOTA-VTI	0.033 0.667	0.656
Positive Clear Lake Shores USA	95° 02′ 06.6″ W 29° 32′ 55.5″ N 16 m	P. Stuart	20.3 cm Watec 910BD IOTA-VTI	0.034 0.718	0.650
(c) 2019-06-04—Stellar occultation by (502) Europa					
Positive CP Cambrune Peru	70° 40′ 42.5″ W 16° 49′ 41.3″ S 3305 m	E. Meza	212.0 cm ZWO ASI178MM GPS	0.075 …	0.587

Table 6
(Continued)

Status Station Country	Longitude Latitude Altitude	Observers	Telescope Aperture CCD Timing	Single Cycle Time (s) Stacked Cycle Time (s)	Light Curve rms
Negative San Pedro de Atacama Chile	68° 10′ 48.0″ W 22° 57′ 08.0″ S 2397 m	A. Maury	15.5 cm STX-16803 GPS	3.570 …	0.610
No detection Oliveira Brazil	43° 59′ 03.1″ W 19° 52′ 55.0″ S 982 m	C. Jacques	45.0 cm ML FLI16803 GPS	1.690 …	2.169
Target saturated Vitoria Brazil	40° 19′ 00.0″ W 20° 17′ 52.0″ S 26 m	M. Malacarne	35.0 cm SBIG/ST-8X-ME NTP	8.000 …	…
Weather overcast Ponta Grossa Brazil	50° 05′ 56.6″ W 25° 05′ 22.5″ S 910 m	C. L. Perreira M. Emilio	40.0 cm Merlin/Raptor GPS	… …	…
Weather overcast OPD—Brazópolis Brazil	45° 34′ 57.5″ W 22° 32′ 07.8″ S 1864 m	B. Morgado	60 cm Andor/Ixon-EM GPS	… …	…
Weather overcast Guaratinguetá Brazil	45° 11′ 25.0″ W 22° 48′ 34.0″ S 567 m	R. Sfair A. R. Gomes-Júnior O. C. Winter	40 cm Merlin/Raptor GPS	… …	…
(e) 2016-04-13—Stellar occultation by (503) Ganymede					
Positive IRTF—Maunakea Hawaii	155° 28′ 18.0″ W 19° 49′ 34.0″ N 4150 m	E. D'Aversa T. Oliva G. Sindoni	320.0 cm SpeX GPS	2.817 …	0.145
Positive SOAO—Sobaeksan South Korea	128° 27′ 27.6″ E 36° 56′ 03.9″ N 1378 m	T. C. Hinse Y. Kim	61.0 cm ProLine PL16803 NTP	6.048 …	0.066

Appendix B
Light Curves

This section provides the plots of the normalized light curves versus UTC analyzed in this work, see Figures 5 to 21. In total, 17 light curves were obtained during four occultations observed between 2016 and 2021. Here, we exclude the light curves from the 2017 March 31 that were published in Morgado et al. (2019b). The events are listed in inverse chronological order, and the light curves are plotted from the northernmost to the southernmost stations. The date, event, and observer are indicated in the title and label of each figure. The upper panel contains the complete normalized light curve (black dots) and the fitted model (red line). The bottom panels have expanded views of a few seconds centered on the star's immersion and emersion behind the main body. In the upper panel, we also show the light curve before the stacking consecutive images technique (gray line) whenever it was used. The normalization was done so that the flux outside the event would be one and the flux within the event would be zero. We highlight that the target never disappears from the images.

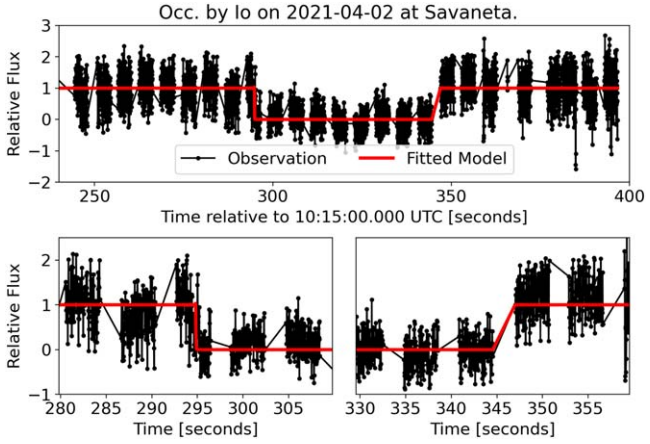


Figure 5. Light curve obtained in Savaneta on 2021 April 2 by J. Vrolijk. The occulting satellite, date, and observational station are indicated in the title and label. The upper panel contains the complete normalized light curve (black dots) and the fitted model (red line). The bottom panels contain zoom-in views of a few seconds, each centered on the immersions and emersions of the star behind the main occulting satellite.

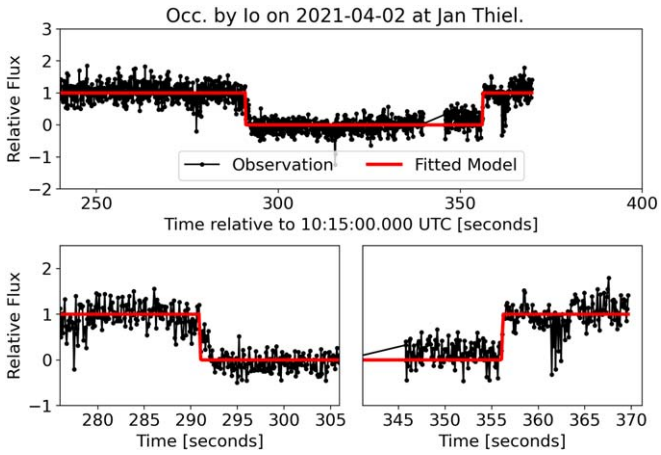


Figure 6. Occ. of Io on 2021 April 2 at Jan Thiel by E. Sussenbach.

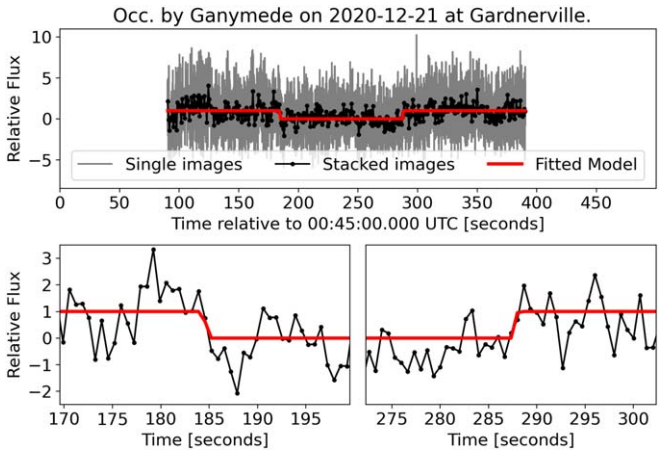


Figure 7. Occ. of Ganymede on 2020 December 21 at Gardnerville by J. Bardecker.

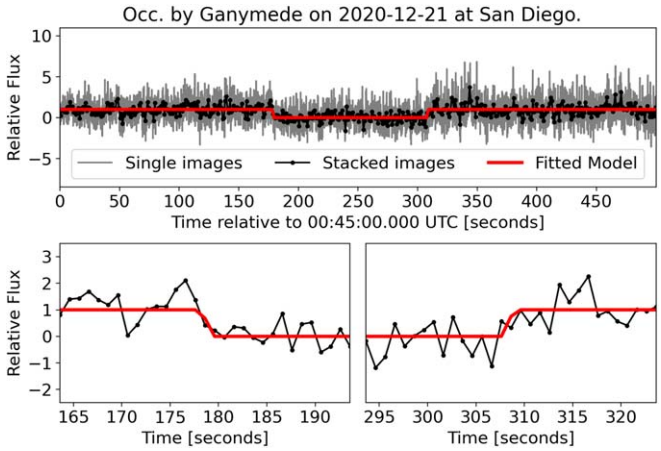


Figure 8. Occ. of Ganymede on 2020 December 21 at San Diego by D. Bruns.

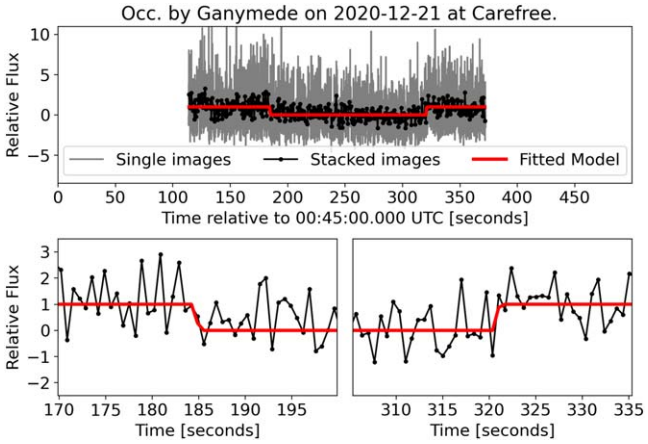


Figure 9. Occ. of Ganymede on 2020 December 21 at Carefree by P. Maley.

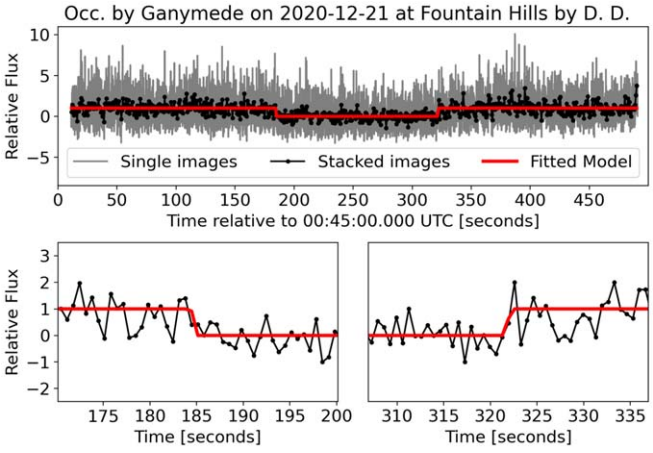


Figure 10. Occ. of Ganymede on 2020 December 21 at Fountain Hills by D. Dunham.

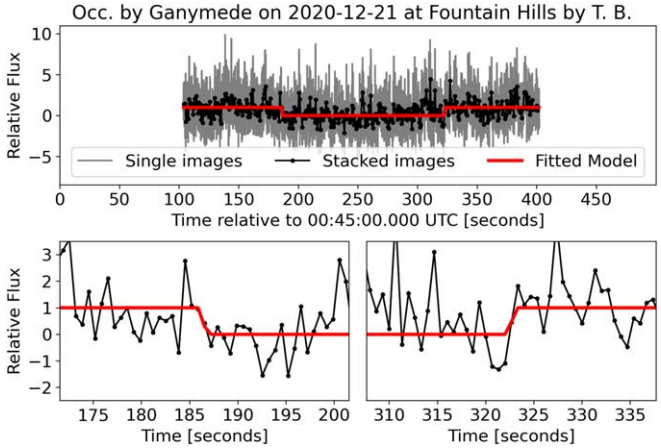


Figure 11. Occ. of Ganymede on 2020 December 21 at Fountain Hills by T. Blank.

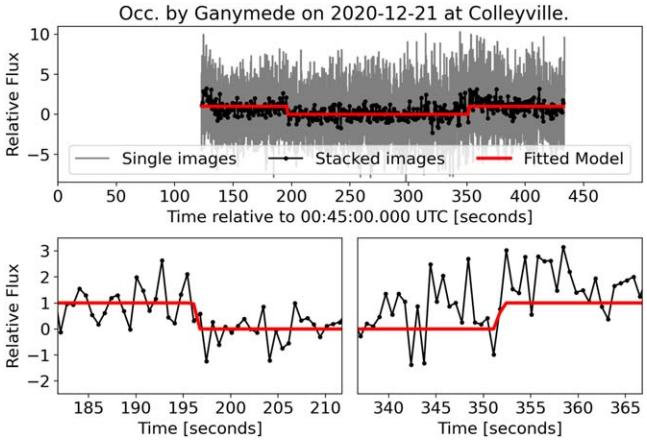


Figure 14. Occ. of Ganymede on 2020 December 21 at Colleyville by M. Smith.

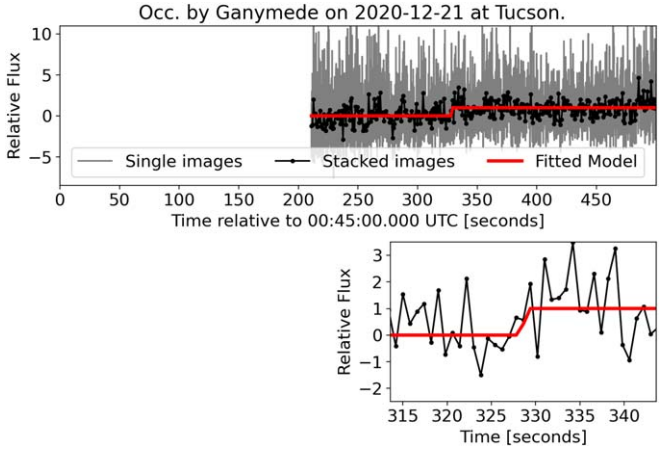


Figure 12. Occ. of Ganymede on 2020 December 21 at Tucson by N. Carlson.

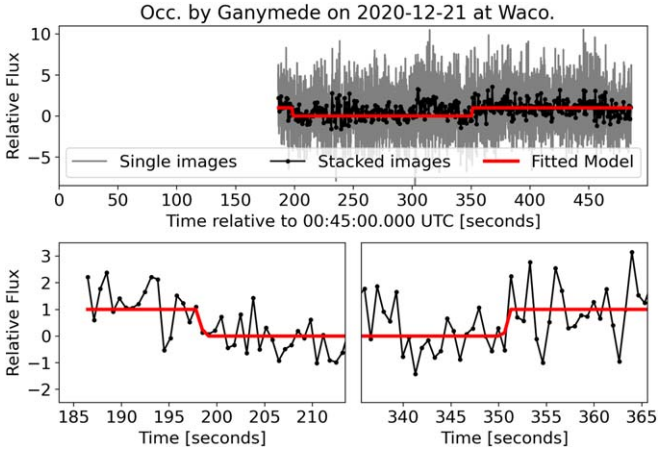


Figure 15. Occ. of Ganymede on 2020 December 21 at Waco by D. Eisfeldt.

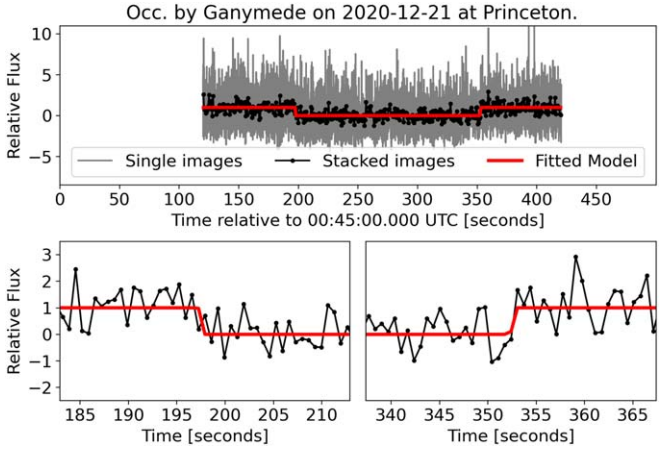


Figure 13. Occ. of Ganymede on 2020 December 21 at Princeton by K. Cobble.

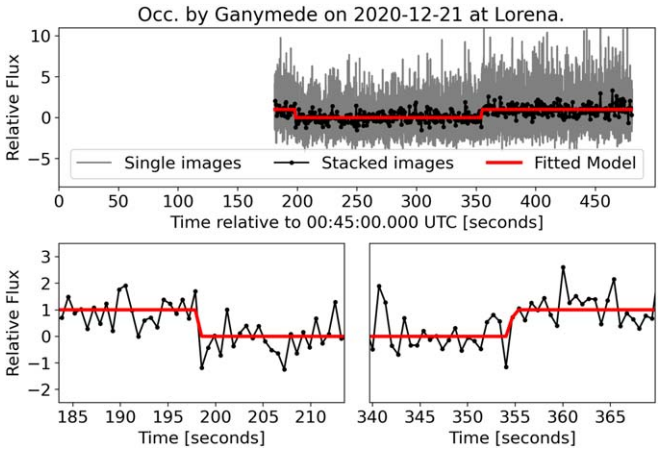


Figure 16. Occ. of Ganymede on 2020 December 21 at Lorena by J. Barton.

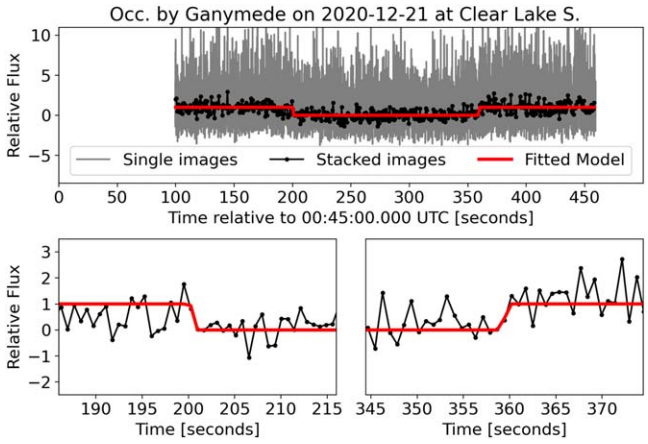


Figure 17. Occ. of Ganymede on 2020 December 21 at Clear Lake Shores by P. Stuart.

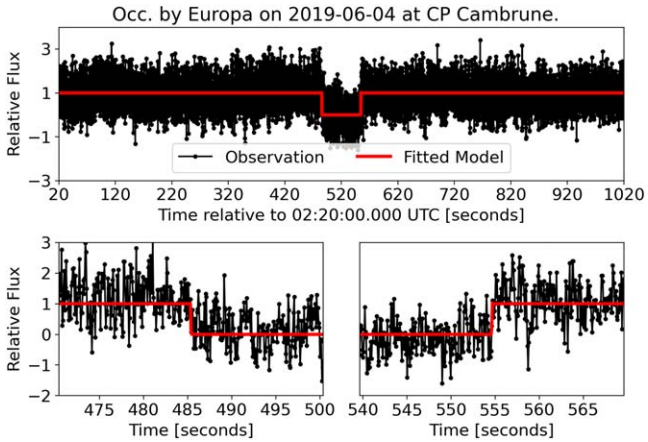


Figure 18. Occ. of Europa on 2019 June 4 at CP Cambrune by E. Meza.

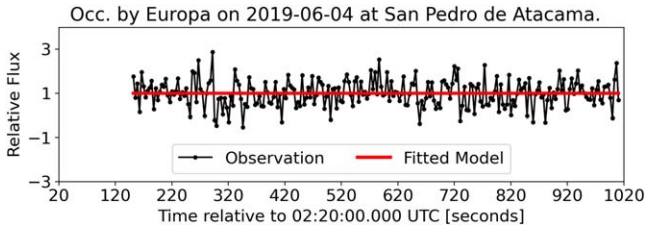


Figure 19. Occ. of Europa on 2019 June 4 at San Pedro de Atacama by A. Maury.

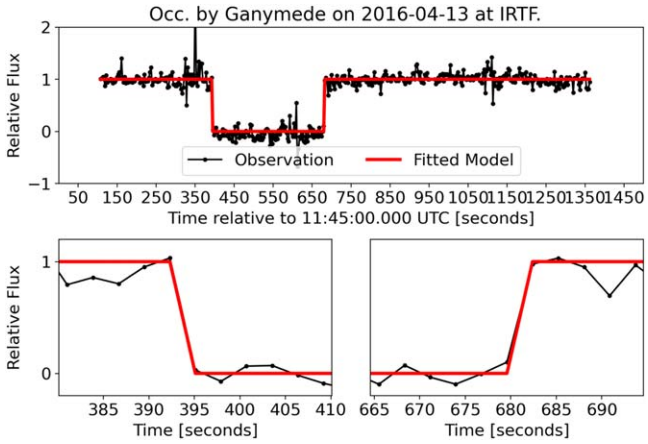


Figure 20. Occ. of Ganymede on 2016 April 13 at IRTF by T. Oliva.

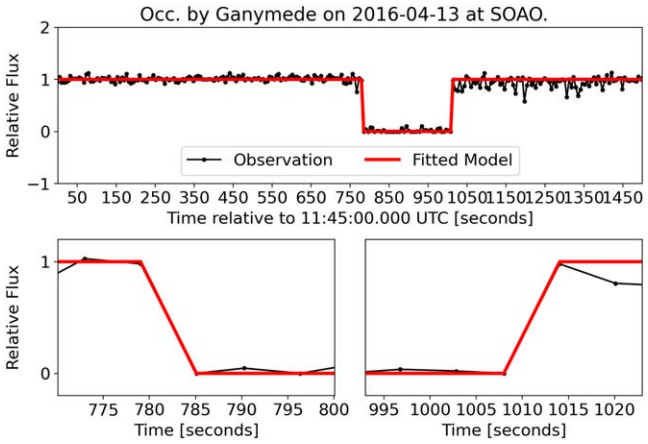


Figure 21. Occ. of Ganymede on 2016 April 13 at SOAO by T. C. Hinse and Y. Kim.

Appendix C
Analysis of the Occultation Observed with the IRTF SpeX Instrument

On 2016 March 14, Ganymede occulted a star of magnitude G 6.99. This occultation was favorable to the Northern Pacific Ocean, Japan, South Korea, and Hawaii. At that epoch, D'Aversa et al. (2017) organized a campaign to observe this event.

This observation aimed to search for a signature of Ganymede's exosphere in the occultation light curve by using the NASA Infrared Telescope Facility (IRTF) on Maunakea (Hawaii). At IRTF, both MIT Optical Rapid Imaging System (MORIS; Gulbis et al. 2011) and SpeX (Rayner et al. 2003) instruments were used, which were fed by the same optical entrance through a dichroic beam splitter at 0.95 microns. The plan was for MORIS to acquire a high-rate sequence of images in the visible range, while SpeX would acquire a series of spectra at a lower rate, covering between 0.9 and 2.5 microns.

The IRTF SpeX data set was obtained between 11:46:47.142 and 12:07:41.851 UTC with a mean cycle of 2.8166 s, resulting in 440 spectra, where the target star and Ganymede were measured in the same aperture. Figure 22 contains three examples of spectra obtained at three instants. In this figure, we also show the spectral range of bands: Y (centered at $\lambda_0 = 1020$ nm with a width $\Delta\lambda = 120$ nm), J ($\lambda_0 = 1220$ nm, $\Delta\lambda = 213$ nm), H ($\lambda_0 = 1630$ nm, $\Delta\lambda = 307$ nm) and K ($\lambda_0 = 2190$ nm, $\Delta\lambda = 390$ nm). We highlight that the instruments' FoV was not large enough to include a reference unocculted body, hence sky fluctuations are the major source of flux variation and noise.

Apart from the IRTF, this occultation was also observed in the Sobaeksan Optical Astronomy Observatory (SOAO) in South Korea. The data set obtained was analyzed using the standard procedures described in Section 2.2. From the SOAO light curve, we determined disappearance and reappearance times of $11{:}58{:}02.028 \pm 2.222$ and $12{:}01{:}51.064 \pm 2.218$. Considering a circle of radius 2631.2 km and the SOAO chord, this would mean that the disappearance and reappearance times of IRTF would be around 11:51:34 and 11:56:19 UTC. However, a direct approach that combines the light flux in all of the spectral regions to provide a raw light curve shows significant flux variation due to sky fluctuations, which precludes the detection of the event, as can be seen in Figure 23. However, as seen in Figure 22, there is a difference

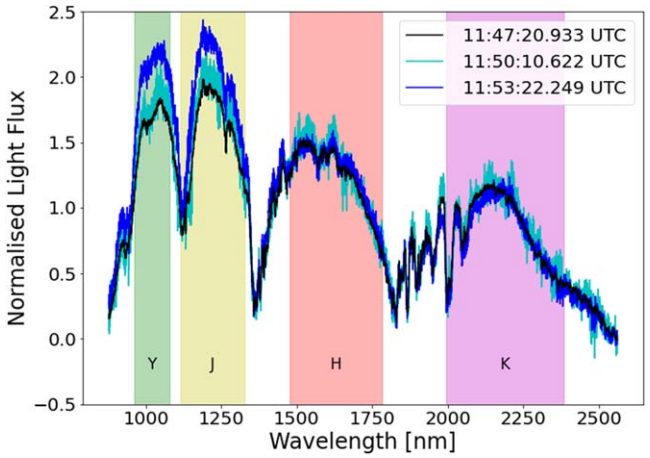


Figure 22. Normalized spectra obtained on the IRTF of the occultation by Ganymede on 2016 April 13. These are the spectra obtained at 11:47:20.933 (in black), 11:50:10.622 (in cyan), and 11:53:22.249 UTC (in blue). We highlight the increase in noise relative to sky fluctuations. This plot also contains the spectral region of the *Y*, *J*, *H*, and *K* bands. For more information, see text.

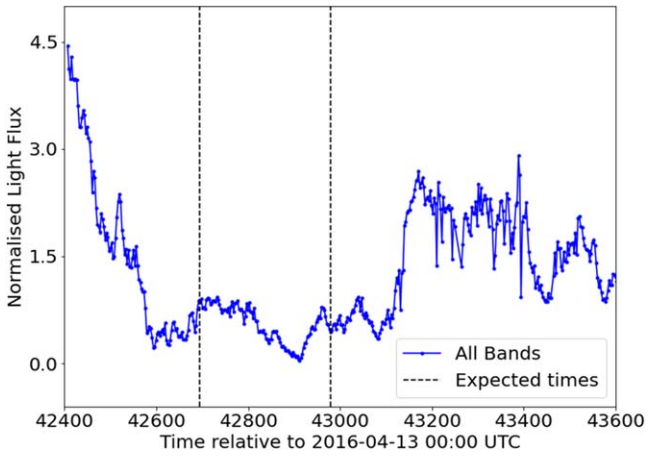


Figure 23. Normalized light curve obtained on the IRTF of the occultation by Ganymede on 2016 April 13. All of the spectra were summed for each instant resulting in a light flux. Note that there is a significant flux variation due to sky fluctuations, which precludes the detection of the event.

between the spectra outside the expected occultation times (cyan and black lines) and the spectra within the expected occultation times (blue line).

A different approach is to use the color curves of this data set, as described in the main text. The expected magnitudes of the occulted star are J 5.549, H 5.176, and K 4.908 (NOMAD-1 catalog, Zacharias et al. 2004). Meanwhile, the expected magnitudes of Ganymede in these filters are J 4.045, H 4.145, and K 4.225, based on a *V* magnitude of 5.045 for the occultation epoch, as obtained using the JPL Horizons service, and the colors provided by Cox & Pilachowski (2000). From these values, we can calculate the magnitude drop (ΔM_i) for a standard magnitude band *i* using Equation (C1).

$$\Delta M_i = M_{\circ i} - M_{\star i} + 2.5\log(1 + 10^{0.4(M_{\star i} - M_{\circ i})}), \qquad \text{(C1)}$$

where $M_{\circ i}$ stands for the magnitude of the occulting body and $M_{\star i}$ is the magnitude of the occulted star, both in band *i*. For example, the occultation in the *J* band would have a magnitude drop of about 0.24, whereas, in the *H* band, it would be 0.35.

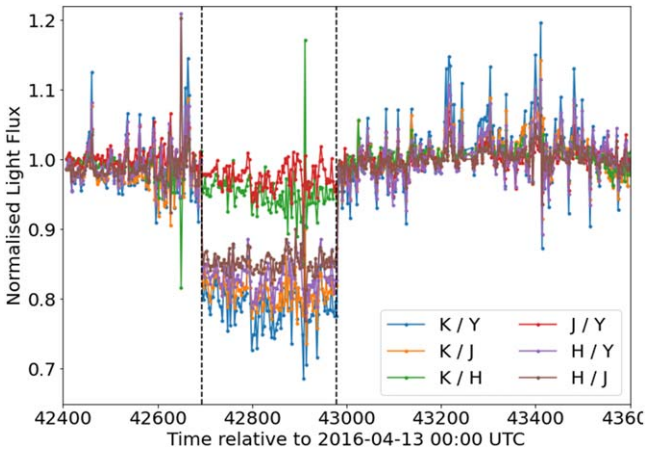


Figure 24. Normalized light curve obtained on the IRTF of the occultation by Ganymede on 2016 April 13. Here, we plot the ratio between fluxes for each specific band (Y, J, K, and H). The disappearance and reappearance times are clearly captured in four ratios with either *Y* or *J* bands at the denominator (H/Y, H/J, K/Y, and K/J), while these times are visually indistinguishable for the other ratios (J/Y and K/H). The dashed-vertical lines represent the expected times. We highlight the agreement between the expected times and the visual drops.

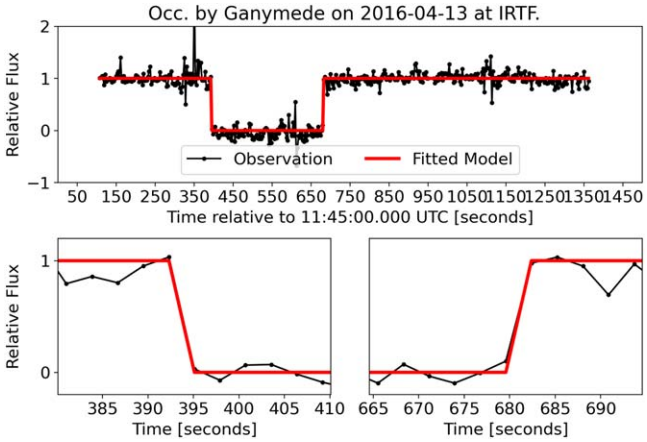


Figure 25. Normalized light curve ,obtained on the IRTF of the occultation by Ganymede on 2016-04-13. Here, we show the color curve relative to the ratio of the bands H/J in black and the fitted modified occultation model in red. The bottom panels contain a zoom-in on 30 s, centered on the immersion and emersion times.

Table 7
Fitted Times Obtained for Each Band Ratio

Band ratio	Immersion time UTC hh:mm:ss.ss (s)	Emersion time UTC hh:mm:ss.ss (s)	χ^2_{pdf}
K/Y	11:51:33.73 (1.23)	11:56:21.12 (1.23)	0.915
K/J	11:51:33.74 (1.23)	11:56:21.02 (1.26)	0.921
H/Y	11:51:33.74 (1.22)	11:56:21.06 (1.27)	0.900
H/J	11:51:33.72 (1.22)	11:56:20.94 (1.24)	0.965

Figure 24 shows six possible ratios considering the magnitudes Y, J, H, and K. We call attention to the fact that the occultation can be seen in four of the flux ratios. This difference can be used to determine the occultation instants without a photometric calibration because we can use one band as a calibrator for another.

Based on the flux ratios, we can fit the disappearance or reappearance time using a similar approach as explained in

Section 2.2. However, instead of using a standard model, we now use the ratio of two models, one for each band. The effect of the stellar diameter in this modified model would be negligible once it affects both models in the same manner. The fitted times using different flux ratios are equivalent, as can be seen in Table 7.

Figure 25 shows the normalized light curve considering the H/J flux ratio and its best fitted model, here the total flux from the star and occulting satellite was normalized to unity outside the occultation and to zero within the occultation. We chose to use the times as obtained from the H/J flux ratios together with the SOAO chord in the limb fit, thus obtaining the astrometric result following the procedure described in Section 2.3 to obtain the result described in Section 3.

We highlight that the color curves allowed us to determine the occultation instants with high accuracy even without a standard photometric calibrator. This was possible because we are using the relative fluxes, so sky transparency is attenuated because it affects the analyzed bands in a similar manner, even though the sky transparency was not ideal. This result emphasizes the efficacy of this method, which can be applied to other scientific cases.

ORCID iDs

B. E. Morgado https://orcid.org/0000-0003-0088-1808
A. R. Gomes-Júnior https://orcid.org/0000-0002-3362-2127
F. Braga-Ribas https://orcid.org/0000-0003-2311-2438
E. D'aversa https://orcid.org/0000-0002-5842-5867
M. Assafin https://orcid.org/0000-0002-8211-0777
B. Sicardy https://orcid.org/0000-0003-1995-0842
T. C. Hinse https://orcid.org/0000-0001-8870-3146
C. L. Pereira https://orcid.org/0000-0003-1000-8113
R. Sfair https://orcid.org/0000-0002-4939-013X
O. C. Winter https://orcid.org/0000-0002-4901-3289

References

Aksnes, K., & Franklin, F. A. 1976, AJ, 81, 464
Aksnes, K., Franklin, F., Millis, R., et al. 1984, AJ, 89, 280
Archinal, B. A., Acton, C. H., A'Hearn, M. F., et al. 2018, CeMDA, 130, 22
Arlot, J.-E., Emelyanov, N., Varfolomeev, M. I., et al. 2014, A&A, 572, A120
Assafin, M., Vieira Martins, R., Camargo, J. I. B., et al. 2011, in Gaia Follow-up Network for the Solar System Objects : Gaia FUN-SSO Workshop Proc. (Paris: IMCCE), 85
Astropy Collaboration, Robitaille, T. P., Tollerud, E. J., et al. 2013, A&A, 558, A33
Brozović, M., Nolan, M. C., Magri, C., et al. 2020, AJ, 159, 149
Butkevich, A. G., & Lindegren, L. 2014, A&A, 570, A62
Cantat-Gaudin, T., & Brandt, T. D. 2021, A&A, 649, A124
Carlson, R. W., Bhattacharyya, J. C., Smith, B. A., et al. 1973, Sci, 182, 53
Charnoz, S., Crida, A., Castillo-Rogez, J. C., et al. 2011, Icar, 216, 535
Cox, A. N., & Pilachowski, C. A. 2000, PhT, 53, 77
Crida, A., & Charnoz, S. 2012, Sci, 338, 1196
D'Aversa, E., Oliva, F., Sindoni, G., et al. 2017, EPSC, 2017, EPSC2017-850
Dirkx, D., Lainey, V., Gurvits, L. I., et al. 2016, P&SS, 134, 82
Dirkx, D., Gurvits, L. I., Lainey, V., et al. 2017, P&SS, 147, 14
Emelyanov, N. V. 2009, MNRAS, 394, 1037
Gaia Collaboration, Prusti, T., de Bruijne, J. H. J., et al. 2016a, A&A, 595, A1
Gaia Collaboration, Brown, A. G. A., Vallenari, A., et al. 2016b, A&A, 595, A2
Gaia Collaboration, Brown, A. G. A., Vallenari, A., et al. 2018, A&A, 616, A1
Gaia Collaboration, Brown, A. G. A., Vallenari, A., et al. 2021, A&A, 649, A1
Gomes-Júnior, A. R., Assafin, M., Beauvalet, L., et al. 2016, MNRAS, 462, 1351
Gomes-Júnior, A. R., Morgado, B. E., Benedetti-Rossi, G., et al. 2022, MNRAS, 511, 1167
Gulbis, A. A. S., Bus, S. J., Elliot, J. L., et al. 2011, PASP, 123, 461
Herald, D., Gault, D., Anderson, R., et al. 2020, MNRAS, 499, 4570
Hubbard, W. B., & van Flandern, T. C. 1972, AJ, 77, 65
Kiseleva, T. P., Izmailov, I. S., Kiselev, A. A., et al. 2008, P&SS, 56, 1908
Lainey, V., Arlot, J.-E., Karatekin, Ö., et al. 2009, Natur, 459, 957
Lainey, V., Karatekin, Ö., Desmars, J., et al. 2012, ApJ, 752, 14
Lainey, V., Jacobson, R. A., Tajeddine, R., et al. 2017, Icar, 281, 286
Morgado, B., Assafin, M., Vieira-Martins, R., et al. 2016, MNRAS, 460, 4086
Morgado, B., Vieira-Martins, R., Assafin, M., et al. 2019a, MNRAS, 482, 5190
Morgado, B., Benedetti-Rossi, G., Gomes-Júnior, A. R., et al. 2019b, A&A, 626, L4
Morgado, B., Vieira-Martins, R., Assafin, M., et al. 2019c, P&SS, 179, 104736
Nimmo, F., Thomas, P. C., Pappalardo, R. T., et al. 2007, Icar, 191, 183
Press, W. H., Teukolsky, S. A., Vetterling, W. T., et al. 1992, Numerical Recipes: The Art of Scientific Computing (2nd ed.; Cambridge: Cambridge Univ. Press)
Rayner, J. T., Toomey, D. W., Onaka, P. M., et al. 2003, PASP, 115, 362
Saquet, E., Emelyanov, N., Robert, V., et al. 2018, MNRAS, 474, 4730
Sicardy, B., Ortiz, J. L., Assafin, M., et al. 2011, Natur, 478, 493
Thomas, P. C., Simonelli, D., Burns, J., et al. 1997, in 28th Annual Lunar and Planetary Science Conf. (Houston, TX: Lunar and Planetary Institute), 1429
Tody, D. 1986, Proc. SPIE, 627, 733
White, O. L., Schenk, P. M., Nimmo, F., et al. 2014, JGRE, 119, 1276
Zacharias, N., Monet, D. G., Levine, S. E., et al. 2004, BAAS, 36, 1418
Zubarev, A., Nadezhdina, I., Oberst, J., et al. 2015, P&SS, 117, 246